Review of Scientific Instruments

Oblique-incidence Sagnac interferometric scanning microscope for studying magneto-optic effects of materials at low temperatures

Cite as: Rev. Sci. Instrum. **92**, 043706 (2021); https://doi.org/10.1063/5.0042574
Submitted: 31 December 2020 . Accepted: 19 March 2021 . Published Online: 08 April 2021

X. D. Zhu, R. Ullah, and V. Taufour

Review of Scientific Instruments ARTICLE scitation.org/journal/rsi

Oblique-incidence Sagnac interferometric scanning microscope for studying magneto-optic effects of materials at low temperatures

Cite as: Rev. Sci. Instrum. 92, 043706 (2021); doi: 10.1063/5.0042574
Submitted: 31 December 2020 • Accepted: 19 March 2021 •
Published Online: 8 April 2021

X. D. Zhu,[a] R. Ullah, and V. Taufour

AFFILIATIONS

Department of Physics and Astronomy, University of California, Davis, California 95616, USA

[a]Author to whom correspondence should be addressed: xdzhu@physics.ucdavis.edu

ABSTRACT

We describe an *oblique-incidence* zero-area Sagnac interferometric microscope for studying spatial and temperature dependence of magneto-optic (MO) effects in samples under cryogenic conditions. The microscope is capable of independently measuring Kerr effects from three Cartesian components of a magnetization and thus can be used to map out the magnetization vector across the sample. For illustration, we present MO Kerr effect images of magnetic domains at 77 K of a $LaCrGe_3$ crystal terminated with an *a*–*c* plane (the plane that contains the lattice *a*-axis and *c*-axis). We further present measurements of magnetization in these domains from 90 to 77 K during zero-field cooling and field cooling in an external magnetic field from 20 to 150 Oe. The inherently high sensitivity and the capability of detecting a magnetization without external modulation makes such a Sagnac interferometric microscope particularly useful for studying magnetic effects in novel materials at low temperatures.

I. INTRODUCTION

The state of magnetic ordering in a bulk or at a surface of a solid under conditions such as temperature, pressure, composition, and external fields is among the most important characteristics of materials. For single crystalline materials, naturally occurring or artificially fabricated, a sample usually consists of domains that can exhibit distinct magnetic ordering, particularly in the absence of sufficiently large external magnetic fields. The dimension of these domains varies from as small as a few nm to as large as a few mm.[1–8] For basic understanding and practical applications, it is desirable to characterize the properties of individual domains as well as behaviors averaged over all domains. This calls for experimental methods that have the capability to measure the magnetic properties of a material in a spatially resolved manner. Magneto-optic (MO) probes based on optical responses to magnetization in a material answer such a call.[7,9–11] MO probes detect the change in polarization state of a reflected (Kerr effect) and transmitted (Faraday effect) light beam induced by the magnetization. Although not as sensitive as SQUID-based methods (but more so than VSM-based methods), optical methods have the advantage of being able to spatially revolve magnetic properties of a sample with resolutions only limited by the wavelength of the light. Mainly there are two types of magneto-optic microscopes. One type employs 2D photodetector arrays for measurement and does not modulate the magnetization for signal extraction.[7,12] This type of microscope, suffering from the 1/f noise and non-magnetic, polarization-altering backgrounds, is used to image samples exhibiting Kerr angles significantly larger than 10 μrad.[13,14] The second type employs some form of modulation in the magnetization for signal extraction and involves a single detector or a pair of balanced detectors for detection at the frequency of modulation or the higher harmonics.[15–17] For this type of microscope, the image acquisition requires scanning the illumination beam across a sample. The scanning microscopes of this type, though slow in image acquisition, can detect MOKE signals as small as 0.1 μrad.[18] Without modulating the magnetization in a sample, non-magnetic backgrounds such as linear birefringence in the optical system and the sample usually limit the MOKE detection sensitivity to 10 μrad.[13,19]

In this work, we describe a scanning MOKE microscope that does not require modulating sample magnetization for signal generation. It is based on zero loop-area Sagnac interferometry at oblique

incidence.[20,21] In this microscope, non-magnetic backgrounds are suppressed by symmetry while magneto-optic effects are doubled. By modulating the phase of the illuminating optical beam, the MOKE signals are detected in the MHz range so that the 1/f noise is below the amplifier noise. The sensitivity of this Sagnac interferometry based MOKE detection is a fraction of 1 μrad and limited by the amplifier noise.[22] The oblique-incidence geometry enables separate measurements of longitudinal, transverse, and polar Kerr effects[21] and in turn the orientation of the magnetization vector in a spatially resolved manner. To illustrate such a Sagnac interferometric MOKE microscope, we studied magneto-optic effects from $LaCrGe_3$ single crystals. In particular, we present images of magnetic domains of $LaCrGe_3$ crystals in a range of external magnetic field and magnetization curves from these domains around the Curie point $T_c = 86$ K[23] from 90 K down to 77 K. We choose $LaCrGe_3$ because the structure of its magnetic domains has so far not been reported in the literature. More importantly, the material exhibits rich magnetic phases below 86 K and under pressures[24–26] and is open to further investigation beyond the present work.

II. OBLIQUE-INCIDENCE ZERO-AREA SAGNAC INTERFEROMETRIC MICROSCOPE (OI-ZASIM)

The principle of oblique-incidence zero-area Sagnac interferometry has been described and demonstrated recently by one of us.[21] In this work, we describe a particular configuration of scanning microscopy based on this principle so that it can be used to image samples in a cryostat through an optical window. Figure 1 shows a schematic diagram of the oblique-incidence zero-area Sagnac interferometric microscope used in this work.

A 25-mW broad-band light beam with the center wavelength at $\lambda = 780$ nm and a bandwidth of 30 nm passes through a polarizing circulator and is focused into a short polarization-maintaining (PM) fiber. The transmission axis (TA) of the circulator is aligned parallel to the slow axis (SA) of the fiber. The other end of the fiber is coupled to an electro-optic modulator (EOM). The SA of the fiber bisects the transverse magnetic (TM) and transverse electric (TE) axes of the EOM. The EOM is a phase modulator made of $LiNbO_3$ with $V_\pi = 1.3$ V (EOSPACE, Inc., Redmond, WA). We apply a sinusoidal wave form to the EOM with an amplitude of 0.35 V at a time frequency $f = 4.445$ MHz (the angular frequency $\Omega = 2\pi f = 2.7915 \times 10^7$ rad/s). This adds a phase shift $\Phi(t) = \Phi_0 \cos(\Omega t)$ with $\Phi_0 = 0.85$ rad to the polarization component of the beam parallel to the TM axis. After the EOM, the phase-modulated beam is coupled into a 10-m PM fiber with the TM axis of the EOM aligned parallel to the SA axis of the fiber. The beam emerges from the fiber and is collimated with a collimation lens to yield a beam with a diameter $d = 4$ mm. The SA of the 10-m PM fiber is set parallel to the horizontal plane. The outgoing beam passes through a first wave plate and is focused on the sample (through a 1.57-mm thick fused quartz window) with an objective lens ($f_1 = 100$ mm, workingdistance (W.D.) = 34 mm) at an oblique incidence angle $\theta_{inc} = 20°$. The diffraction-limited resolution is $\delta_l = \lambda f_1/d = 20\,\mu$m, in good agreement with the experimental value of $\delta_{l,exp} = 25\,\mu$m. The choice of 20° is deliberate as will be clear shortly. After reflection, the beam passes through the same objective lens to become collimated again. It continues through a second wave plate and is then focused on a reflection mirror with a second objective lens ($f_2 = 20$ mm, W.D. = 33.5 mm). The mirror sends the beam all the way back to the polarizing circulator to complete the Sagnac loop that encloses no area. The circulator further sends the returned beam (with a total power of a few μW) to a 120-MHz bandwidth photoreceiver (New Focus Model-1801, Newport Corp., CA) with a gain of 2×10^4 V/W at 780 nm. The voltage signal generated in the photoreceiver is analyzed with two lock-in amplifiers that yield Fourier components in the intensity of the returned

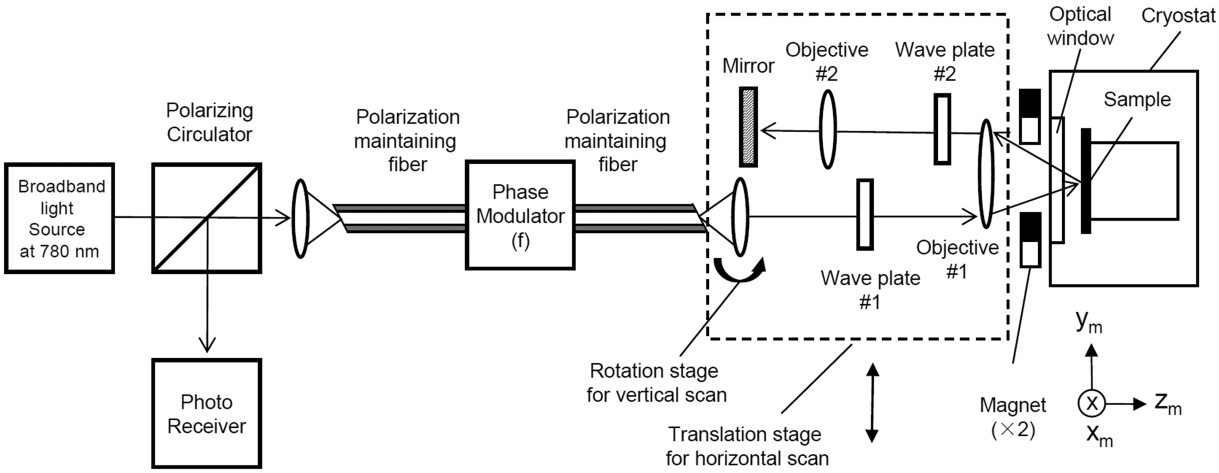

FIG. 1. An arrangement of oblique-incidence zero-area Sagnac interferometric microscope (OI-ZASIM) for measuring longitudinal, transverse, and polar Kerr angles of a magnetic sample. Optical elements in the dotted box are mounted on a linear stage so that the beam spot on the sample can be scanned along the horizontal direction. The collimation lens is mounted on a rotation stage so that the pitch angle of the beam can be changed to the beam spot on the sample vertically. Two permanent magnets are placed outside a cryostat (Janis ST-500, Lakeshore Scientific, NJ) to produce a variable in-plane magnetic field at the sample along the horizontal or vertical direction.

beam at the first and second harmonic of the phase modulation frequency f.

Let $P_{10} = \begin{bmatrix} 1 \\ 0 \end{bmatrix}$ and $P_{20} = \begin{bmatrix} 0 \\ 1 \end{bmatrix}$ be the Jones vectors for the two linearly polarized components of the optical beam that emerges from the 10-m PM fiber: one along the SA of the PM fiber (i.e., the p-polarization with respect to the sample) and the other along the fast axis (FA) of the fiber (i.e., the s-polarization). They are transformed to two different and yet still orthogonally polarized components $P_1 = \begin{bmatrix} a \\ be^{i\varphi} \end{bmatrix}$ and $P_2 = \begin{bmatrix} b \\ -ae^{i\varphi} \end{bmatrix}$ (with $\sqrt{a^2 + b^2} = 1$) after the first wave plate. Let

$$M = \begin{bmatrix} m_{11} & m_{12} \\ m_{21} & m_{22} \end{bmatrix} \tag{1}$$

be the Jones matrix that includes effects from all optical elements encountered by the "beam" as it traverses to and back from the sample and returns to the first wave plate. The matrix elements have terms that vary linearly with three Cartesian components of the sample magnetization. The measurable Sagnac signal is the differential phase given by[21]

$$\alpha_K = 2\theta_K = Arg\left\{\frac{[ab(m_{11} - m_{22}e^{i2\varphi}) + (b^2 - a^2)(m_{21} + m_{12})e^{i\varphi}/2] - (m_{21} - m_{12})e^{i\varphi}/2}{[ab(m_{11} - m_{22}e^{i2\varphi}) + (b^2 - a^2)(m_{21} + m_{12})e^{i\varphi}/2] + (m_{21} - m_{12})e^{i\varphi}/2}\right\}. \tag{2}$$

The Kerr angle θ_K is a combination of Kerr rotation and Kerr ellipticity, depending upon the optical elements in the Sagnac loop and the state of polarization after the first wave plate. To measure α_K, we note that the first and the second harmonics at the angular frequency of phase modulation Ω (rad/s) in the returned beam intensity are[21]

$$I(\Omega) \cong (\gamma/2)I_{inc}\left|ab\left(m_{11} - m_{22}e^{i2\varphi}\right) + \left(b^2 - a^2\right) \times (m_{21} + m_{12})e^{i\varphi}/2\right|^2 J_1(2\Phi_0)\alpha_K, \tag{3}$$

$$I(2\Omega) \cong (\gamma/2)I_{inc}\left|ab\left(m_{11} - m_{22}e^{i2\varphi}\right) + \left(b^2 - a^2\right) \times (m_{21} + m_{12})e^{i\varphi}/2\right|^2 J_2(2\Phi_0), \tag{4}$$

where I_{inc} is the power of the light source right before entering the polarizing circulator and γ is the overall throughput due to passing through all the optical elements in the Sagnac loop. From the experimental value of $I(\Omega)$ and $I(2\Omega)$, we deduce the Kerr angle[21]

$$\theta_K = \left(\frac{1}{2}\right)\frac{I(\Omega)}{I(2\Omega)}\frac{J_2(2\Phi_0)}{J_1(2\Phi_0)}, \tag{5}$$

where θ_K is a linear function of three Cartesian components of magnetization. The polar Kerr angle $\theta_{K,P}$ is proportional to the z_m component that is out-of-plane and pointing into the sample (see Fig. 1); the longitudinal Kerr angle $\theta_{K,L}$ is proportional to the y_m component that is the in-plane component inside the incident plane; and the transverse Kerr angle $\theta_{K,T}$ is the x_m component that is the other in-plane component but perpendicular to the incident plane.

For the scanning microscope in this study, we choose the following combinations of optical elements to separately measure three Kerr angles. For the longitudinal Kerr angle $\theta_{K,L}$, we use a half-wave plate for the first wave plate with the fast axis (FA) set to 22.5° from the p-polarization so that $a = b = 1/\sqrt{2}$ and $\varphi = 0$. For the second wave plate after the sample, we use a quarter-wave plate with its FA set parallel to the p-polarization. At an incidence angle of 20°, the reflectivities for s-polarization and p-polarization have nearly the same amplitude and are 180° out of phase, i.e., $r_s = -r_p$. This is one of the reasons behind choosing $\theta_{inc} = 20°$. From Eq. (18) in Ref. 21, we arrive at (see the supplementary material)

$$\theta_{K,L} \cong Re\left\{\frac{2\sin\theta_{inc}Q}{\varepsilon_s - 1}\right\}m_y, \tag{6}$$

where Q is the dimensionless Voigt parameter. It is complex for opaque samples. ε_s is the dielectric constant at the wavelength of the light source (780 nm in this case). m_y is the directional cosine of the magnetization along the y_m axis.

For the transverse Kerr angle $\theta_{K,T}$, we remove the first wave plate so that $a = 1$, $b = 0$, and $\varphi = 0$. For the second wave plate, we use a quarter-wave plate with its FA set to be +45° rotated from the p-polarization. From Eq. (21) in Ref. 21, we have (see the supplementary material)

$$\theta_{K,T} \cong Re\left\{\frac{2\sin\theta_{inc}Q}{\varepsilon_s - 1}\right\}m_x, \tag{7}$$

where m_x is the directional cosine of the magnetization along the x_m axis. Since the scaling factor $Re\left\{\frac{2\sin\theta_{inc}Q}{\varepsilon_s - 1}\right\}$ is the same for the transverse Kerr angle and the longitudinal Kerr angle, we only need to calibrate this factor by saturating the magnetization in one direction with a sufficiently large external magnetic field.

For the polar Kerr angle $\theta_{K,P}$, we choose a quarter-wave plate for the first wave plate with its FA set to +45° from the p-polarization so that $a = b = 1/\sqrt{2}$ and $\varphi = 90°$. We remove the second wave plate entirely. From Eq. (15) in Ref. 21, again it is easy to show (see the supplementary material)

$$\theta_{K,P} \cong Im\left\{\frac{2\sqrt{\varepsilon_s}Q}{\varepsilon_s - 1}\right\}m_z. \tag{8}$$

We particularly note that for transparent magnetic materials, $Im\left\{\frac{2\sqrt{\varepsilon_s}Q}{\varepsilon_s - 1}\right\} = 0$ and $Re\left\{\frac{2\sin\theta_{inc}Q}{\varepsilon_s - 1}\right\} \neq 0$. In these cases, this

microscope can only be used to measure in-plane components of the magnetization. However, if the magnetization is from a single domain, we can deduce m_z from $\sqrt{m_x^2 + m_y^2 + m_z^2} = 1$.

As shown in Fig. 1, the sample is mounted on a cold stage inside a Janis ST-500 cryostat. The latter is fixed to an optical table for stability. To acquire a Kerr angle image, we scan the focused beam position on the sample. To vary the horizontal position of the beam on the sample, we mount the fiber collimation lens and optical elements afterward, except for the sample, on an encoded linear stage with precision and repeatability better than $\Delta x = 0.5\,\mu$m. To vary the vertical position of the beam, we mount the fiber collimation lens on a backlash-free rotary stage with a stepping motor so that the pitch angle δ_p of the beam can be varied reproducibly. The vertical beam movement on the sample surface (also the focal plane of the first objective) as a function of the pitch angle δ_p is simply

$$y \cong f_1 \delta_p. \tag{9}$$

In the present scanning microscope, the step size of the pitch angle is limited by the stepping motor to 1°/400 or $\Delta\delta_p = 4.25 \times 10^{-5}$ rad. With $f_1 = 100$ mm, this yields a linear step size $\Delta y = 4.25\,\mu$m.

We now elaborate on the second reason for choosing $\theta_{inc} = 20°$. Since the returned beam is focused back into the PM fiber with the same collimation lens, distortions of the beam by optical elements after the lens can significantly reduce the coupling efficiency back into the fiber. In fact, the coma aberration introduced by transmission through the optical window at oblique incidence is the major source of distortion. Although $\theta_{inc} = 0°$ would be best for reducing coma distortion to nearly zero, the normal incidence geometry does not measure longitudinal and transverse Kerr angles as are evident from Eqs. (6) and (7). The optimal choice is near $\theta_{inc} = 20°$ where the back-coupling efficiency is close to the maximum.

III. MAGNETIC DOMAINS IN $LaCrGe_3$ SINGLE CRYSTALS BELOW THE CURIE TEMPERATURE T_c

We next describe a series of measurements using this Sagnac interferometric scanning microscope on $LaCrGe_3$. The crystal has a hexagonal perovskite structure (space group P63/mmc). It becomes ferromagnetically ordered along the lattice c-axis at 86 K under ambient pressure.[23] Our $LaCrGe_3$ samples are synthesized in house from high purity (>3 N) elements of La, Cr, and Ge. They are premixed by arc-melting in a ratio of La:Cr:Ge = 13:13:74. The ingot is loaded into an alumina crucible and sealed in a fused silica tube under a partial pressure of high purity argon gas. The ampoule containing the mixed material is heated up to 1100 °C over 3 h and then held at 1100 °C for another 3 h to allow growth to take place. The after-growth material is slowly cooled to 825 °C over 65 h. The excess liquid is decanted with a centrifuge during cool down. We select two crystals that expose high quality *a*–*c* planes. From the morphology of the samples, we can identify the lattice *c*-axis on the surface. The samples are fixed with a colloidal silver paint to the cold stage and the latter is mounted inside the cryostat. Using liquid nitrogen as a cryogenic coolant, the temperature of the cold stage can be controlled and ramped between 470 and 77.4 K. To apply an external magnetic field from the outside of the cryostat, we use a pair of 20-mm diameter, coaxially aligned $Nd_2Fe_{14}B$ permanent magnets that are separated by 45 mm. The field is aligned along the horizontal direction and thus parallel to the y_m axis. By changing the vertical

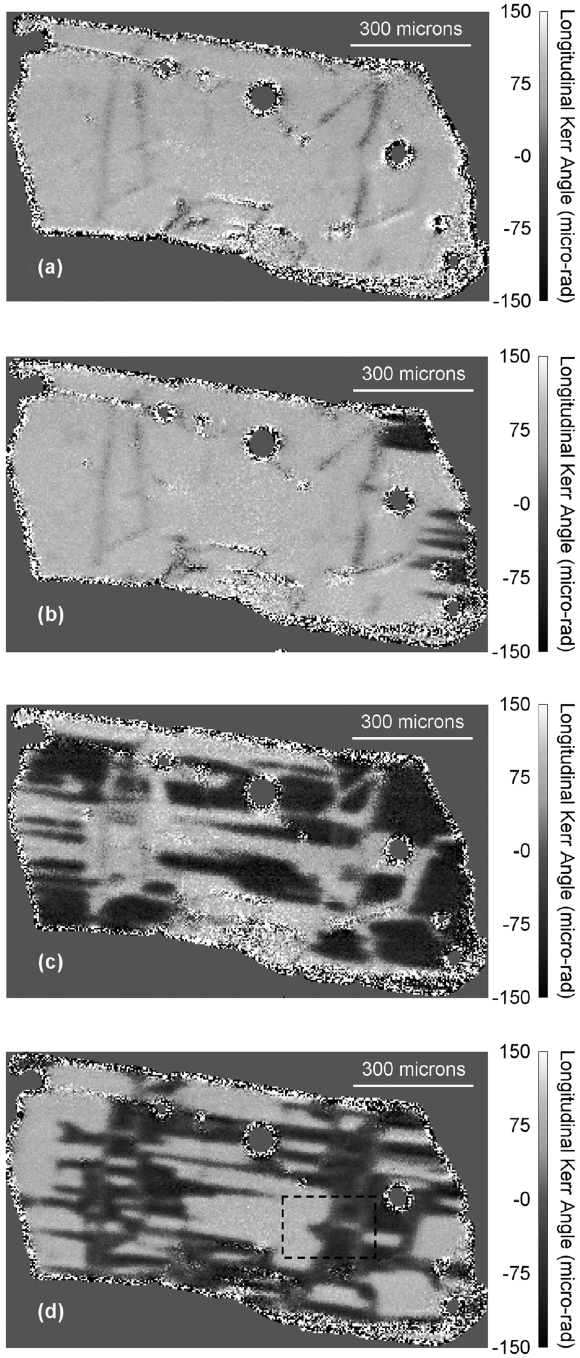

FIG. 2. (a) Image in longitudinal Kerr angle $\theta_{K,L}$ of a 1200 × 800 μm^2 on the *a*–*c* plane of one $LaCrGe_3$ crystal, acquired after cooling from 90 to 77.4 K in an in-plane magnetic field H = 150 Oe applied to the right. (b) Image in longitudinal Kerr angle $\theta_{K,L}$ of the same 1200 × 800 μm^2 area after cooling from 90 to 77.4 K in a magnetic field H = 40 Oe applied to the right. (c) Image in longitudinal Kerr angle $\theta_{K,L}$ of the same 1200 × 800 μm^2 area after cooling from 90 to 77.4 K in a magnetic field H = 20 Oe applied to the right. (d) Image in longitudinal Kerr angle $\theta_{K,L}$ of the same 1200 × 800 μm^2 area after cooling from 90 to 77.4 K in zero magnetic field. The region enclosed by the box is further imaged in longitudinal and transverse Kerr angles (see Fig. 3) to determine the orientation of magnetic domains.

distance of the magnet pair from the sample, we vary the magnitude of the magnetic field from below that of the Earth field to 260 Oe.

Figure 2 shows the images in longitudinal Kerr angle of the *a*–*c* plane from one $LaCrGe_3$ crystal after it is cooled down from 90 to 77.4 K in different magnetic fields. The fields are in the horizontal direction to the right of the images: (a) H = 150 Oe, (b) H = 40 Oe, (c) H = 20 Oe, and (d) H = 0 Oe. The sizes of the images are 1200 × 800 μm^2. The step size in both directions is 4.25 μm. At T = 90 K (above the Curie temperature),[23] the images (not shown) are featureless and serve as the background. They are subtracted from images acquired at 77.4 K. The difference images (shown in Fig. 2) are proportional to the y_m component of the sample magnetization at 77.4 K. For the purpose of display, we set the phase of the lock-in amplifier so that the longitudinal Kerr angle $\theta_{K,L}$ is positive when the magnetization is aligned in the direction of the applied magnet field to the right. The fuzzy features on the surface are defects and protrusions with facets other than the *a*–*c* plane. We note that the lattice *c*-axis is along the long edge of the sample, thus not parallel to the horizontal direction. It is tilted clockwise by roughly 5°.

At H = 150 Oe, $\theta_{K,L}$ is more or less uniform across the sample and has a positive amplitude of 90 ± 12 μrad. It indicates that the directional cosine of the magnetization m_y is uniformly aligned in the direction of the applied field. When the field strength is reduced to 40 Oe, $\theta_{K,L}$ remains uniform except for small pockets on the right where it becomes negative. The latter signals that magnetic domains with opposite alignments start to emerge. As the field is further reduced to 20 Oe, $\theta_{K,L}$ is no longer uniform and the sample consists of oppositely aligned domains that are tens to hundreds of micrometers in size. $\theta_{K,L}$ in "dark" regions have a negative amplitude of 90 ± 12 μrad, indicating that the opposite alignment of m_y in these domains is complete. When there is no external field at all during cool down from 90 to 77.4 K, the sample again breaks into domains of magnetizations with m_y either aligned to the right or to the left. Shapes and sizes of the domains change (as long as the external field is less than 20 Oe) from measurement to measurement, depending upon the history of heating and cooling cycles, particularly the external fields used during the cycles.

To fully determine the orientation of magnetic domains shown in Fig. 2, we need to know the directional cosine m_x of these domains. An image in transverse Kerr angle reveals just such information. In Fig. 3, we show images in longitudinal Kerr angle $\theta_{K,L}$ and transverse Kerr angle $\theta_{K,T}$ acquired back to back from a region of 230 × 150 μm^2 [the boxed region in Fig. 2(d)]. The amplitude of $\theta_{K,T}$ in the middle of the domains is 8–14 μrad. To acquire the image with signal-to-noise ratio (SNR) ≈10, we used a time constant of 1 s for averaging so that the amplifier-limited noise is reduced to ±1.2 μrad (i.e., ±0.000 07°). The arrows indicate the directions of m_y and m_x. The ratio of Figs. 3(b) and 3(a), $m_x/m_y = \tan\phi$, yields the tilt angle ϕ of the magnetization from the horizontal axis to the right. For clarity, the absolute value of ϕ is shown in Fig. 3(c). As shown by the arrows, the magnetization tilts clockwise from the horizontal direction by 6°–10° in the bright region and is in the opposite direction in the dark region. It shows that magnetic domains are indeed aligned either parallel or anti-parallel to the lattice *c*-axis in the absence of an external magnetic field or when the strength of the external field is less than 20 Oe.

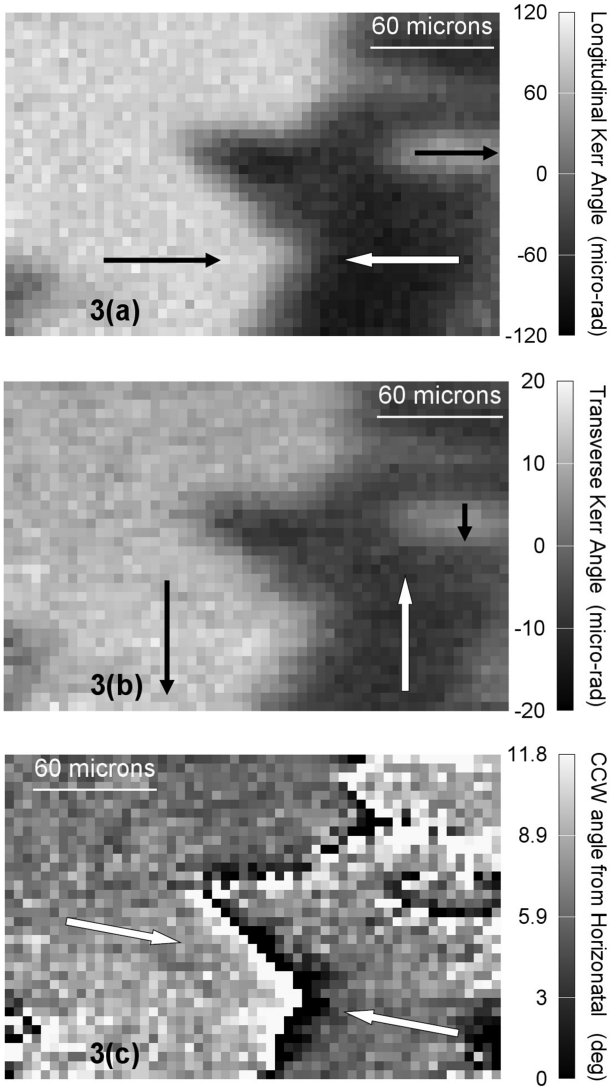

FIG. 3. (a) Image in longitudinal Kerr angle $\theta_{K,L}(proportionalto\, m_y)$ of a 230 × 150 μm^2 area, as marked in Fig. 2(d), after ZFC from 90 to 77.4 K. (b) Image in transverse Kerr angle $\theta_{K,T}(proportionalto\, m_x)$ from the same 230 × 150 μm^2 area after a subsequent ZFC from 90 to 77.4 K. (c) The amplitude of $\phi = \tan^{-1}(\theta_{K,T}/\theta_{K,L})$ from the horizontal direction to the right. The arrows indicate the actual direction of magnetization in the *a*–*c* plane. They are either parallel or anti-parallel to the lattice *c*-axis.

We note that because images shown in Figs. 3(a) and 3(b) are acquired back to back instead of during the same scan, the mechanical drift in the microscope system causes the domain boundary in Fig. 3(a) where $m_y = 0$ to shift slightly from the boundary in Fig. 3(b) where $m_x = 0$. As a result, the image in $\tan^{-1}(m_x/m_y)$ clearly reveals the domain boundary as the bright line where $m_y = 0$ or the dark line where $m_x = 0$.

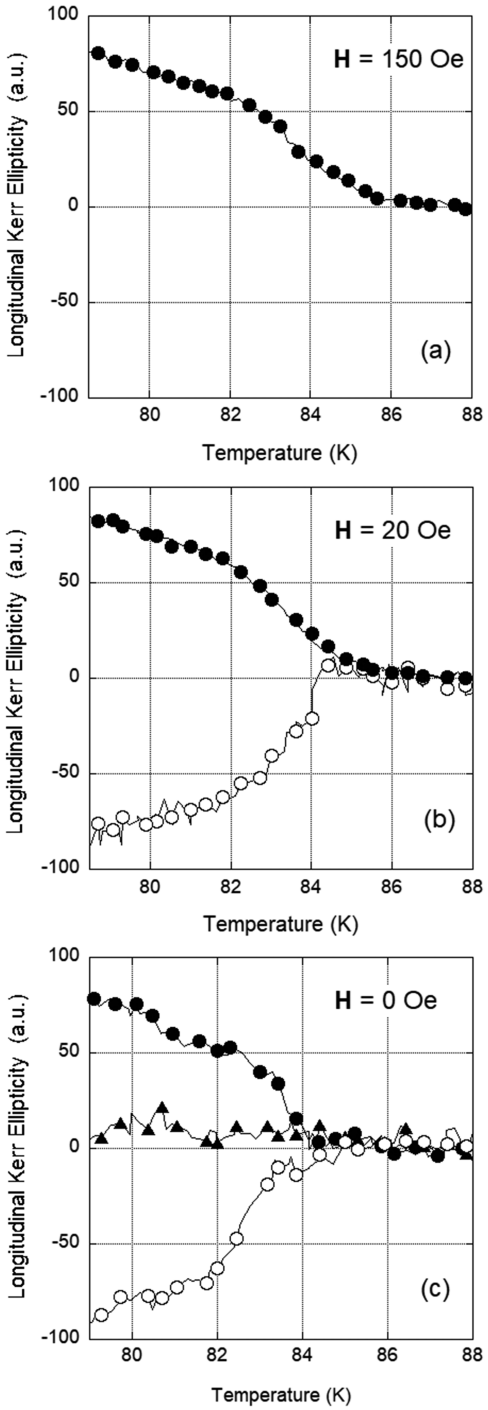

FIG. 4. (a) Magnetization curve during field cooling at 150 Oe from a location inside a domain with m_y aligned along the applied field. (b) Magnetization curves during field cooling at 20 Oe: (1) full circles (●) from a domain with m_y aligned along the applied field and (2) empty circles (○) from a domain with m_y aligned opposite to the applied field. (c) Magnetization curves during zero-field cooling: (1) full circles (●) from a domain with m_y aligned to the right [see Fig. 3(a)], (2) empty circles (○) from a domain with m_y aligned to the left [see Fig. 3(a)], and (3) triangles (▲) from the vicinity of a domain boundary.

IV. MAGNETIZATION FROM DIFFERENT DOMAINS DURING ZERO-FIELD COOLING AND FIELD-COOLING

To examine the magnetization of different magnetic domains in the $LaCrGe_3$ sample near the Curie point (T_c = 86 K), we cool the sample from 90 K down to 77.4 K, and at every 0.1 K decrement, we measure $\theta_{K,L}$ at locations close to the middle of domains or a domain boundary. Figure 4 shows a set of measured $\theta_{K,L}$ during field-cooling (FC) in a constant external magnetic field at (a) H = 150 Oe, (b) H = 20 Oe, and (c) H = 0 Oe [zero-field cooling (ZFC)].

At 150 Oe, m_y from the entire sample increases from zero in the direction of the applied field as the temperature decreases below 86 K. It shows that the external field is sufficiently large to overcome the crystalline anisotropy along the lattice *c*-axis. Figure 4(a) shows a representative curve from the middle of the sample. At 20 Oe, the field is no longer strong enough to overcome the crystalline anisotropy. m_y from some region of the sample still increases with a dropping temperature below 86 K but in the direction opposite to the applied field. Figure 4(b) shows one curve from a domain with m_y aligned along the applied field and one from a domain with m_y pointing opposite to the field. When there is no external field present, the sample breaks into domains with opposite alignments along the lattice c-axis and m_y either increases or decreases as the temperature drops below 86 K. m_y changes much less near a domain boundary due to spatial average of m_y over the beam size ($\delta_{l,exp}$ = 25 μm). Figure 4(c) shows one curve from a domain having m_y aligned to the right, one from a domain with m_y aligned to the left, and one from the vicinity of a domain boundary.

By fitting the magnetization curves in Figure 4(b) to a function of $\theta_{K,L}(T) = \theta_{K,L,Max}(1 - T/T_c)^{\alpha}$, we obtain $T_c = 84.3 \pm 0.2$ K, $\alpha = 0.49 \pm 0.08$, and $\theta_{K,L,Max} = 330 \pm 50$ μrad. The measured Curie temperature is closed to and, in fact, slightly lower than the value reported in the literature.[23]

V. DISCUSSION

In this study, $LaCrGe_3$ is used to illustrate the capability of our oblique-incidence Sagnac interferometric scanning microscope for investigating the spatial and temperature dependence of magnetic properties of a sample. It is motivated by the fact that the crystal displays rich magnetic phases at temperatures below 86 K and under pressure. The present microscope enables further investigation of some of these phases from a single magnetic domain. Images of magnetic domains in a $LaCrGe_3$ single crystal have not been reported before to the best of our knowledge. As these domains are tens of micrometers perpendicular to the *c*-axis while hundreds of micrometers along the *c*-axis, the magneto-optic optical microscope is thus suitable for characterizing ferromagnetic phases of $LaCrGe_3$ as a function of temperature, spatial locations, and maybe even pressure.

A. Characterization of the full orientation of magnetic domains of $LaCrGe_3$

We demonstrated one of the most useful utilities of the present scanning microscope, that is, by acquiring images of m_x and m_y from the same area, we can completely determine the in-plane orientation of magnetic domains of the $LaCrGe_3$ sample. The in-plane orientation of a magnetization can be measured without having to calibrate the proportionality constant in Eqs. (6) and (7). It is because the

ratio $\theta_{K,T}/\theta_{K,L}$ is a trivial trigonometric function of the in-plane orientation and contains no other unknown parameter. For materials that do have an out-of-plane component m_z, this microscope can measure it by directly detecting the polar Kerr angle given in Eq. (8) (after suitable calibration to find the proportionality constant $\mathrm{Im}\left\{\frac{2\sqrt{\varepsilon_s}Q}{\varepsilon_s-1}\right\}$). If the proportionality constant is small or zero as is the case for transparent materials or difficult to determine due to insufficient external magnetic field perpendicular to the sample surface, one can alternatively calibrate $\theta_{K,L}$ for proportionality constant $\mathrm{Re}\left\{\frac{2\sin\theta_{inc}Q}{\varepsilon_s-1}\right\}$ and find m_z from $\sqrt{m_x^2+m_y^2+m_z^2}=1$.

In the present microscope, the image in $\phi=\tan^{-1}(\theta_{K,T}/\theta_{K,L})$ is subject to mechanical drifts in the scanning system including the cryostat. In the future, one way to ensure that measurements of m_x, m_y, and m_z are done on the same point on a sample is to measure three Kerr angles at one location before moving on to the next so that images in all three Kerr angles are acquired "simultaneously." This would minimize the effect of mechanical drifts that are ubiquitous in an optical scanning microscope when it is combined with a cryostat and a magnet.

B. Spatial resolution

Images acquired in the present study have a resolution determined by the diffraction-limited beam diameter on the sample ($\delta_{l,exp}=25\,\mu$m) and the step size of 4.25 μm. For magneto-optic effects in $LaCrGe_3$, these are sufficient as the size of magnetic domains is much larger. To improve the resolution for samples with significantly smaller magnetic domains, the diffraction-limited beam size can be reduced to 4 μm by increasing the beam size after the collimator from 4 to 20 mm while using the same objective with $f_1=100$ mm, W.D. = 34 mm. The step size can be reduced to 1 μm by using a galvo mirror that can be stepped at 1.0×10^{-5} rad with high repeatability.

C. Sensitivity

We should particularly note that the image in transverse Kerr angle shown in Fig. 3(b) has a noise floor of ±1.2 μrad. This is remarkable for a Kerr angle image of magnetic samples acquired without modulating the magnetization for background reduction.[18] The noise floor is currently limited by the noise equivalent power of the photoreceiver, $NEP=3.3\,\mathrm{pW}/\sqrt{\mathrm{Hz}}$, and the low power in the returned beam at the photoreceiver, $I(2\Omega)=1\mu$W. The low throughput in the present scanning microscope, from an initial 25 mW to a few μW at the photo-receiver, is partly due to the available objectives that are not AR-coated for 780 nm. There are effectively four objectives and the beam passes through each of them twice. The transmittance through one objective is 0.75 for single pass. Together, they reduce the throughput by a factor of 10. By replacing these objectives with ones that are AR-coated for 780 nm so that the single-pass transmittance increases to 0.95, we should be able to increase the beam power at the photoreceiver by a factor of 7 and in turn reduce the noise floor to 0.17 μrad for the image shown Fig. 3(b). Using a photo-receiver with an $NEP=0.7\,\mathrm{pW}/\sqrt{\mathrm{Hz}}$, the minimum detectable Kerr angle will be reduced to below $4\times10^{-8}\,\mathrm{rad}/\sqrt{\mathrm{Hz}}$. High sensitivities without having to modulate sample magnetization make Sagnac interferometric microscopes particularly useful in studying materials that have weak and yet characteristic magnetic signatures such as topological insulators, Dirac Weyl semi-metals, and unconventional superconductors. For materials that have large magneto-optic response, the improved high sensitivity can be utilized for acquiring images over much shorter scan times.

VI. CONCLUSION

We demonstrated a prototypical scanning magneto-optic microscope based on oblique-incidence zero-area Sagnac interferometry. It is readily combined with a cryostat so that magneto-optic effects from materials can be studied at low temperatures. Although the prototype is built with optics of availability instead of optimal choice, it still has the adequate spatial resolution of 25 μm, diffraction-limited by the beam size used in this work, to reveal the magnetic domain structure of the $LaCrGe_3$ crystal for the first time. It has the capability to acquire *separate* images of Kerr effects from all three Cartesian components of sample magnetization so that the orientation of magnetic domains can be fully determined. Furthermore, the present prototype has a remarkable sensitivity of ±1.2 μrad for Kerr angle imaging without modulating sample magnetization. We illustrated these features with a set of measurements on the $LaCrGe_3$ crystal, paving the way for further investigation of this material at lower temperature where it displays rich ferromagnetic phases.

SUPPLEMENTARY MATERIAL

See the supplementary material for derivations of Eqs. (6)–(8) starting from the results reported in Ref. 21 and a picture of the scan head for the oblique-incidence zero-area Sagnac interferometric microscope.

ACKNOWLEDGMENTS

X.D.Z. would like to thank Fudan University for a Visiting Lecture Professorship that supports part of this work.

DATA AVAILABILITY

The data that support the findings of this study are available from the corresponding author upon reasonable request.

REFERENCES

[1] T. Taniuchi, Y. Motoyui, K. Morozumi, T. C. Rodel, F. Fortuna, A. F. Santander-Syro, and S. Shin, Nat. Commun. **7**, 11781 (2016).
[2] C. Dufour *et al.*, Phys. Rev. B **84**, 064420 (2011).
[3] S. Eisebitt, J. Lüning, W. F. Schlotter, M. Lörgen, O. Hellwig, W. Eberhardt, and J. Stöhr, Nature **432**, 885 (2004).
[4] M. H. Burkhardt *et al.*, Phys. Rev. Lett. **108**, 237202 (2012).
[5] X. H. Liu, W. Liu, Z. M. Dai, S. K. Li, T. T. Wang, W. B. Cui, D. Li, A. C. Komarek, C. F. Chang, and Z. D. Zhang, Appl. Phys. Lett. **111**, 212401 (2017).
[6] R. M. Bozorth, J. Phys. Radium **12**, 308 (1951).
[7] J. McCord, J. Phys. D: Appl. Phys. **48**, 333001 (2015).
[8] R. Wang *et al.*, Chin. Phys. Lett. **33**, 047502 (2016).

[9]R. P. Hunt, J. Appl. Phys. **38**, 1652 (1967).
[10]Z. Q. Qiu and S. D. Bader, Rev. Sci. Instrum. **71**, 1243 (2000).
[11]Z. Q. Qiu and S. D. Bader, J. Magn. Magn. Mater. **200**, 664 (1999).
[12]H. Rohrmann and H. Hoffmann, Thin Solid Films **175**, 273 (1989).
[13]I. V. Soldatov and R. Schäfer, Rev. Sci. Instrum. **88**, 073701 (2017).
[14]W. Jiang *et al.*, Nat. Phys. **13**, 162 (2017).
[15]P. Kasiraj, R. Shelby, J. Best, and D. Horne, IEEE Trans. Magn. **22**, 837 (1986).
[16]S. A. Crooker, D. D. Awschalom, and N. Samarth, IEEE J. Sel. Top. Quantum Electron. **1**, 1082 (1995).
[17]S. A. Crooker, D. D. Awschalom, J. J. Baumberg, F. Flack, and N. Samarth, Phys. Rev. B **56**, 7574 (1997).
[18]Y. K. Kato, R. C. Myers, A. C. Gossard, and D. D. Awshalom, Science **306**, 1910 (2004).
[19]J. Liu *et al.*, Meas. Sci. Technol. **30**, 125201 (2019).
[20]A. Fried, M. Fejer, and A. Kapitulnik, Rev. Sci. Instrum. **85**, 103707 (2014).
[21]X. D. Zhu, Rev. Sci. Instrum. **88**, 083112 (2017).
[22]J. Xia, P. T. Beyersdorf, M. M. Fejer, and A. Kapitulnik, Appl. Phys. Lett. **89**, 062508 (2006).
[23]X. Lin, V. Taufour, S. L. Bud'ko, and P. C. Canfield, Phys. Rev. B **88**, 094405 (2013).
[24]V. Taufour *et al.*, Phys. Rev. Lett. **117**, 037207 (2016).
[25]V. Taufour, U. S. Kaluarachchi, S. L. Bud'ko, and P. C. Canfield, Physica B **536**, 483 (2018).
[26]U. Kaluarachchi, S. L. Bud'ko, P. C. Canfield, and V. Taufour, Nat. Commun. **8**, 546 (2017).